Passive cavitation imaging with ultrasound arrays

Vasant A. Salgaonkar, Saurabh Datta, Christy K. Holland, and T. Douglas Mast[a)]
Department of Biomedical Engineering, University of Cincinnati, 231 Albert Sabin Way, Cincinnati, Ohio 45267-0586

(Received 12 January 2009; revised 21 August 2009; accepted 4 September 2009)

A method is presented for passive imaging of cavitational acoustic emissions using an ultrasound array, with potential application in real-time monitoring of ultrasound ablation. To create such images, microbubble emissions were passively sensed by an imaging array and dynamically focused at multiple depths. In this paper, an analytic expression for a passive image is obtained by solving the Rayleigh–Sommerfield integral, under the Fresnel approximation, and passive images were simulated. A 192-element array was used to create passive images, in real time, from 520-kHz ultrasound scattered by a 1-mm steel wire. Azimuthal positions of this target were accurately estimated from the passive images. Next, stable and inertial cavitation was passively imaged in saline solution sonicated at 520 kHz. Bubble clusters formed in the saline samples were consistently located on both passive images and B-scans. Passive images were also created using broadband emissions from bovine liver sonicated at 2.2 MHz. Agreement was found between the images and source beam shape, indicating an ability to map therapeutic ultrasound beams *in situ*. The relation between these broadband emissions, sonication amplitude, and exposure conditions are discussed.
 [DOI: 10.1121/1.3238260]

PACS number(s): 43.60.Fg, 43.35.Ei, 43.80.Vj [CCC] Pages: 3071–3083

I. INTRODUCTION

This paper presents a method for spatially sensitive passive cavitation detection with a conventional ultrasound imaging array. Here, microbubble position is ascertained passively by sensing acoustic emissions with a synthetically focused imaging array. The resulting two-dimensional (2D) maps are referred to as passive cavitation images. Acoustic cavitation may be defined as any observable activity of a bubble population under acoustic stimulation[1] and is often categorized into stable and inertial cavitation.[2] The overall motivation for this work is to map cavitation effects produced during ultrasound ablation. Therapeutic ultrasound fields induce nonlinear bubble oscillations causing subharmonic emissions related to stable cavitation, broadband emissions associated with inertial cavitation,[3] and kilohertz frequency emissions resulting from vaporous boiling.[4] Passive images of these acoustic emissions can provide spatial information about the location and dynamics of an active bubble population.

Microbubble activity is known to play an important role in several ultrasound-based therapeutic applications, some of which are briefly reviewed. In shock-wave lithotripsy, kidney stones are broken by inertially collapsing bubbles that generate shock waves and fluid micro-jets, leading to stone surface erosion and fragmentation.[5–7] Several researchers suggest that micro-streaming due to stable cavitation and micro-jetting due to inertial cavitation enhance thrombolytic mechanisms.[8–10] Ultrasound-induced cavitation also offers the exciting possibility of targeted drug and gene delivery using lipid-coated microbubbles which can encapsulate bioactive materials.[11–13] Cavitation activity occurring during ultrasound ablation of soft tissue[14,15] is postulated to increase ultrasound absorption.[16] This can result in faster treatments but can also complicate energy deposition and distort ablative lesion shapes.[17–20]

Passive cavitation detection methods have been employed to monitor cavitation arising from ultrasound-tissue interaction. During some recent experimental studies on ultrasound ablation with focused and unfocused, continuous-wave (CW) sources, subharmonic and broadband-emission signals, consistent with stable bubble oscillations and inertial collapse, respectively, have been detected passively.[21–23] Some researchers have found significant correlation between broadband-emission levels and tissue echogenicity following soft tissue ablation with high-intensity focused ultrasound (HIFU) sources *in vivo*[24] and unfocused intense ultrasound *in vitro*.[23] *In vitro* studies involving HIFU[25] and unfocused ultrasound[23] have indicated that increased broadband emissions corresponded with increase in the volume of coagulated or necrosed tissue. Another study with HIFU ablation of tissue-mimicking phantoms documents a sudden decrease in broadband-emission levels with the onset of boiling.[21] During tissue boiling, low-frequency (kilohertz) acoustic emissions have also been detected experimentally with both HIFU[4,22] and unfocused intense ultrasound[23] A previous *in vitro* study of bovine liver ablation with unfocused ultrasound found that subharmonic emission levels depended on tissue temperature as well as sonication amplitude.[23] Passive cavitation detection is a promising basis for ultrasound ablation guidance and control.

A typical passive cavitation detection system employs a single-element focused transducer, where the detector focus is aligned with the expected location of cavitation activity. In the case of HIFU ablation, acoustic cavitation and gas formation due to tissue boiling can cause the ablative lesion (tissue coagulation) to grow toward the ultrasound source.[17,20] However, a single-element focused passive detector cannot provide information about position-dependent

[a)]Author to whom correspondence should be addressed. Electronic mail: doug.mast@uc.edu

changes in cavitation activity during ablative lesion formation. An unfocused detector can be used to obtain a bulk recording of acoustic emissions, but at the cost of spatial sensitivity.[23] Multiple detectors interrogating the insonation volume may enable the measurement of position-dependent cavitation. A multi-element detector like an ultrasound array has the potential to provide 2D-resolved measurement of cavitational acoustic emissions. Passive imaging with arrays has been attempted in the detection of subterranean acoustic sources using back-projection and cross-correlation methods.[26] Cross-correlation methods are also under investigation for cavitation imaging during HIFU ablation.[27] These algorithms require a synchronous signal acquisition by array elements. Many conventional ultrasound imaging systems are not designed for passive data capture and their available beamforming methods are not suitable for this kind of imaging. The development of customized beamforming methods is needed for passive cavitation imaging using a diagnostic ultrasound system. Recently, passive imaging was applied in HIFU ablation of tissue phantoms, where a conventional ultrasound array was used in a passive mode by switching off the initial transmit pulse and spatial sensitivity was obtained in the azimuthal direction (normal to the array axis).[21]

This paper describes beamforming methods to scan array subapertures electronically and receive acoustic emission signals sequentially for each receive-focus position. The signal level detected at each focal position gives the brightness value for the corresponding point on a 2D map, called a passive cavitation image. Here, analytic expressions for passive cavitation image formation are described.[28] Simulations of passive cavitation images with different beamforming configurations are shown. Finally, experiments with passive cavitation imaging in phosphate-buffered saline (PBS) and *ex vivo* liver tissue are presented. Passive cavitation methods developed here have potential application in real-time, direct visualization of ultrasound-tissue interaction, particularly in guidance and monitoring of ultrasound ablation.

II. THEORY

In B-mode imaging, ultrasound arrays transmit a short acoustic pulse and the medium is imaged from the resulting echoes. The reflector distance is determined through time-of-flight calculations and the image brightness depends on medium properties such as acoustic impedance and attenuation.[29] In contrast, passive cavitation images as defined here resolve acoustic sources by dynamically focusing their passively detected acoustic emissions. Thus, for passive cavitation imaging, image characteristics such as spatial resolution, contrast, and dependence on imaging system parameters differ from conventional B-mode imaging. Below, analytic expressions are derived for passive cavitation images with aims to elucidate experimental results and optimize imaging system parameters through computer simulations.

A. Signal received by a rectangular array element

To ascertain the emission signal detected by a rectangular array element, a cavitating bubble is modeled as a point-source emitting spherical sound waves and the resulting pressure field is integrated over the element surface. For a pulsating sphere of finite radius a, the volume flow Q of fluid from the source relates to the particle velocity u as[30]

$$Q(t) = 4\pi a^2 \frac{\partial u(a,t)}{\partial r}. \tag{1}$$

In the small-radius limit $a \to 0$, the pressure field at a position $\mathbf{r}$ for the point-source (bubble) radiating in a medium with density ρ and sound speed c is given by[30]

$$p(\mathbf{r},t) = \frac{\rho \dot{Q}(t - |\mathbf{r}|/c)}{4\pi|\mathbf{r}|}. \tag{2}$$

The received emission signal $s_n(t)$ for an element n centered at $\mathbf{r}_0$ (area $\mathbf{S}_0$) due to a bubble at $\mathbf{r_s}$ is obtained by integrating the radiated pressure from Eq. (2) over the element surface. This results in the Rayleigh–Sommerfield integral[31]

$$s_n(t) = \oint \frac{\rho \dot{Q}(t - |\mathbf{r_0} - \mathbf{r_s}|/c)}{4\pi|\mathbf{r_0} - \mathbf{r_s}|} dS_0, \tag{3}$$

which can be expressed in the frequency domain as

$$S_n(\omega) = \frac{-i\omega\rho\dot{\mathcal{Q}}(\omega)}{4\pi} \oint \frac{e^{(i|\mathbf{r_0}-\mathbf{r_s}|\omega/c)}}{|\mathbf{r_0} - \mathbf{r_s}|} dS_0, \tag{4}$$

where ω denotes radial frequency and dS_0 is an area-element on the receiver surface. An approximate solution of the frequency-domain Rayleigh–Sommerfield integral can be obtained using the Fresnel approximation,

$$|\mathbf{r_0} - \mathbf{r_s}| \approx z_s + \frac{(x_s - x_0)^2}{2z_s} + \frac{(y_s - y_0)^2}{2z_s},$$

$$\frac{1}{|\mathbf{r_0} - \mathbf{r_s}|} \approx \frac{1}{z_s}. \tag{5}$$

For an array element with dimensions $2a \times 2b$ focused at depth F_x in elevation and F_y in azimuth, Eq. (4) can be written under the Fresnel approximation as[32]

$$\begin{aligned} S_n(\omega) &= \frac{-i\omega\rho\dot{\mathcal{Q}}(\omega)}{4\pi z_s} e^{ik(z_s^2 + |\mathbf{r_s}|^2)/2z_s} \\ &\quad \times \int_{-a}^{a} e^{ikx_0^2/2F_x} e^{ik(x_0^2 - 2x_0x_s)/2z_s} dx_0 \\ &\quad \times \int_{-b}^{b} e^{iky_0^2/2F_y} e^{ik(y_0^2 - 2y_0y_s)/2z_s} dy_0, \\ &= \frac{-i\omega\rho\dot{\mathcal{Q}}(\omega)\Phi(\mathbf{r_s},k)}{4\sqrt{\tilde{k}_x}\sqrt{\tilde{k}_y}} \left(\mathbf{F}\left[\frac{kx_s + \tilde{k}_x a}{\sqrt{\pi\tilde{k}_x z_s}} \right] \right. \\ &\quad \left. - \mathbf{F}\left[\frac{kx_s - \tilde{k}_x a}{\sqrt{\pi\tilde{k}_x z_s}} \right] \right) \times \left(\mathbf{F}\left[\frac{ky_s + \tilde{k}_y b}{\sqrt{\pi\tilde{k}_y z_s}} \right] \right. \\ &\quad \left. - \mathbf{F}\left[\frac{ky_s - \tilde{k}_y b}{\sqrt{\pi\tilde{k}_y z_s}} \right] \right), \end{aligned} \tag{6}$$

where the wave number $k=\omega/c$, $\tilde{k}_x=k(1-z_s/F_x)$, and $\tilde{k}_y=k(1-z_s/F_y)$. $\mathbf{F}$ is the complex Fresnel integral which is given by $\mathbf{F}(\zeta)=\int_0^\zeta e^{i\pi u^2/2}du$. The multiplicative term Φ is expressed as $\Phi(\mathbf{r_s},k)=\exp(ik[z_s^2+|\mathbf{r_s}|^2-k(x_s^2/\tilde{k}_x+y_s^2/\tilde{k}_y)]/(2z_s))$.

B. Analytic expression for passive images

In the passive cavitation imaging method presented here, acoustic emissions are spatially resolved through synthetic focusing of array subapertures at multiple depths. For simplicity, a subaperture may be approximated as a single, uniform, continuous rectangular transducer, which produces a voltage proportional to the received acoustic pressure, integrated over the element surface.[31] The brightness value for a passive image point (Y,Z) is defined as the total beamformed energy from a group of acoustic sources sensed by a subaperture which is focused at that point,

$$I(Y,Z)=\sum_{\forall\omega}|S(\omega,Y,Z)|^2, \tag{7}$$

where ω is the radial frequency of a single radiating frequency component and the symbol $\forall$ ("for all") indicates summation over all radiating frequencies. In the case of stably cavitating bubbles, these correspond to discrete harmonics, subharmonics, and ultraharmonics of the sonication frequency.

To obtain the point-spread function for a passive cavitation image, an expression for the received signal $S(\omega,Y,Z)$ due to a single source at (x_s,y_s,z_s) is obtained by idealizing the linear array to have small pitch, no edge limits, and continuous receive focusing, so that an N-element subaperture can be represented by a single rectangular transducer of length $2b\times N$:

$$\begin{aligned}S(\omega,Y,Z)=&\frac{-A_0 i\omega\rho\dot{Q}(\omega)\Phi(\mathbf{r_s},k)}{4\sqrt{\tilde{k}_x}\sqrt{\tilde{k}_y}}\\&\times\left(\mathbf{F}\left[\frac{kx_s+\tilde{k}_x a}{\sqrt{\pi\tilde{k}_x z_s}}\right]-\mathbf{F}\left[\frac{kx_s-\tilde{k}_x a}{\sqrt{\pi\tilde{k}_x z_s}}\right]\right)\\&\times\left(\mathbf{F}\left[\frac{ky_s-Y+\tilde{k}_y bN}{\sqrt{\pi\tilde{k}_y z_s}}\right]\right.\\&\left.-\mathbf{F}\left[\frac{ky_s-Y-\tilde{k}_y bN}{\sqrt{\pi\tilde{k}_y z_s}}\right]\right),\end{aligned} \tag{8}$$

where $\tilde{k}_y=k(1-z_s/Z)$ and Φ is as defined for Eq. (6).

C. Passive images by time-delay focusing

To model the point-spread function of a passive cavitation image created using time-delay receive beamforming, the signal received by an individual array element [Eq. (6) with $F_y\to\infty$] is subjected to an appropriate delay. Time-delayed, received signals from all elements in a subaperture are summed to obtain the beamformed emission signal. To focus a subaperture with N elements on its axis at depth Z, the time delay applied to the nth element is given by

$$\tau_n=\frac{-Z-\sqrt{(y_n-Y)^2+Z^2}}{c}. \tag{9}$$

The beamformed emission signal, corresponding to an image brightness value, is then expressed as

$$I(\omega,Y,Z)=\sum_{\forall\omega}\left|\sum_{\forall n}e^{i\omega\tau_n}S_n(\omega)\right|^2. \tag{10}$$

III. SIMULATIONS

The theory discussed above was used to simulate passive cavitation images using MATLAB 7.1 (Mathworks Inc., Natick, MA) software. Simulations were performed for the 192-element, 7.5-MHz center frequency linear array (L7, Ardent Sound, Mesa, AZ) employed in the experiments reported below. Each element on this array is 0.195 mm in azimuth and 7.0 mm in elevation, with pitch 0.22 mm and a constant focal depth of 25 mm in elevation. The maximum allowable subaperture dimension for the imaging system employed here is 64-elements, spanning 14.08 mm. The minimum subaperture size was set to 8-elements, spanning 1.76 mm. The imaging system allowed discrete receive-focusing to be performed in 16 distinct focal zones. Received signals due to cavitational emissions were computed from Eq. (6) using a rational approximation to the complex Fresnel integral.[33]

A. Simulated passive images of a point-source

Simulated passive images are first shown for a single point-source located on the array axis at 20-, 55-, or 90-mm depth. The simulated sources were modeled to emit acoustic energy at harmonics of 520-kHz between 5.2 and 9.36 MHz. This choice of fundamental frequency, harmonic components, and frequency bandwidth is consistent with the harmonic scattering experiments described below. Beamforming of emissions was simulated using Eq. (6) for a 14.08-mm subaperture and image brightness was computed by summing beamformed emission energy for each harmonic according to Eq. (7).

Images shown in the top row of Fig. 1 were simulated using Eq. (6) for an idealized subaperture with continuous receive-focusing and no truncation at the array edges. Images in the bottom row of Fig. 1 were created by time-delay beamforming the received signal energy, as given in Eq. (10). Receive foci were placed at 16 distinct depths separated by 6.2 mm. The total image depth was 101 mm and subaperture sizes were truncated at the array edges. For example, the 32nd A-line was formed by beamforming the received signals from elements 1–64, but the 4th A-line was comprised of signals received by elements 1–8. All these parameters were consistent with specifications of the ultrasound imaging system used in the experiments reported in Sec. IV. Figure 2 shows simulated images of a point-source created with a constant f-number (ratio of receive-focus depth to subaperture width) subaperture, while the other imaging parameters were same as Fig. 1. It can be seen from Fig. 1 that the brightness pattern narrows or converges at the point-source depth, while it broadens at greater or lesser depths.

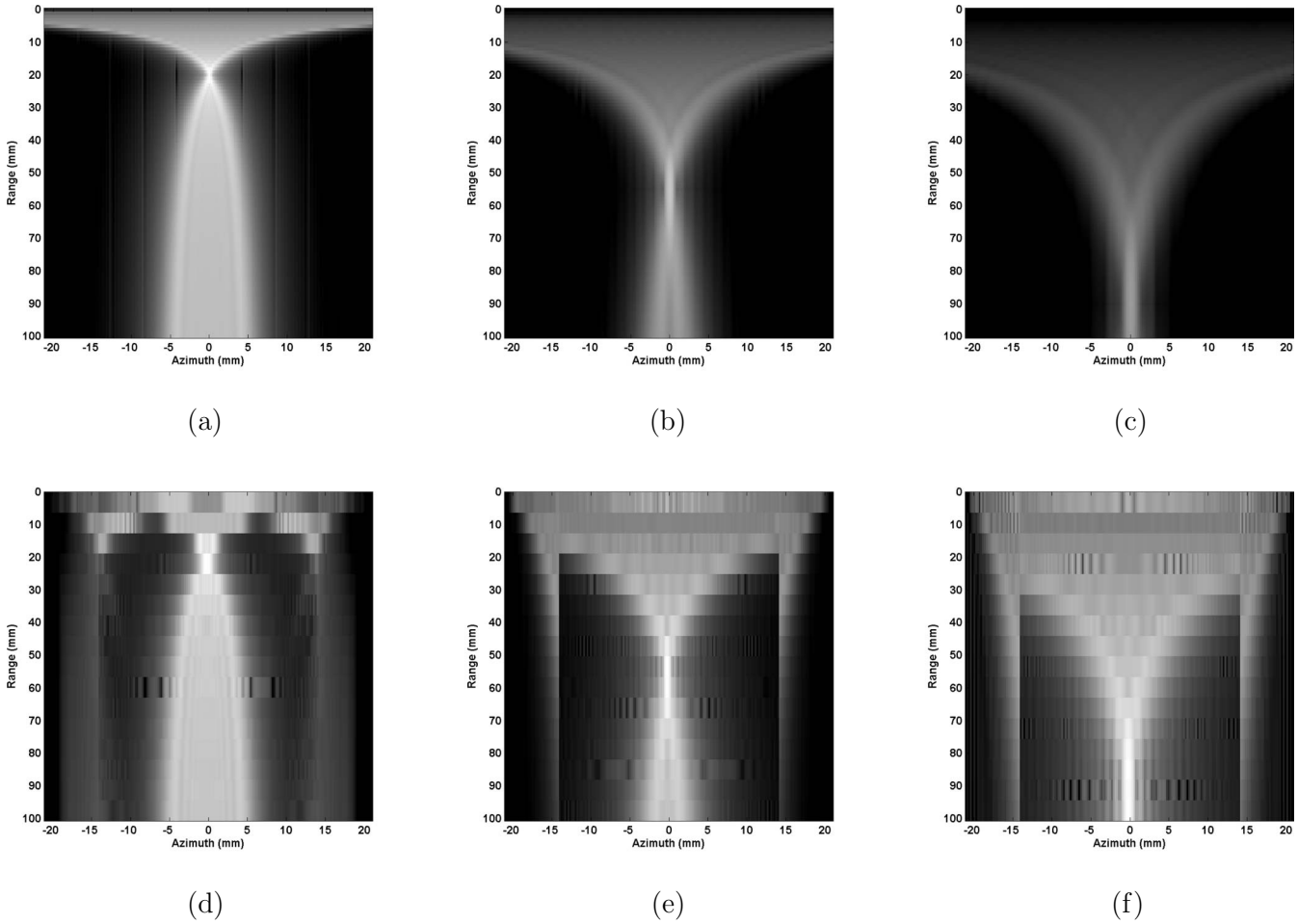

FIG. 1. Computer simulations for passive images created using 64-element (14.08 mm) subapertures are shown here. The top row contains examples of simulations where an "idealized" array approximation is used for each subaperture, with single point-sources at depths (a) 20 mm, (b) 55 mm, (c) and 90 mm. Simulated images in the bottom row were created through time-delay focusing at 16 equally spaced depths (6.2 mm) with single point-sources located at (d) 20 mm, (e) 55 mm (e), and (f) 90 mm. All images are plotted with a 40 dB dynamic range.

This is true for both "idealized" and time-delay approaches. With a constant f-number, the corresponding image shows similar characteristics but the brightness pattern on the image converges at a greater depth than the point-source range.

The beamforming configuration influences image resolution depending on the size of the synthetic focus. A good measure for this is the −6-dB beam width of the receiver sensitivity pattern of the subaperture in the azimuthal direction. The imaging array is assumed to have a fixed focus in elevation (similar to the L7 array employed in the experiments described below). The focus size in the azimuthal direction changes with subaperture size and focal depth, and can be approximated by the focal width of an unapodized line aperture.[29] For a wavelength λ, the −6-dB width for an N-element subaperture is thus approximated as

$$W_{-6\text{-dB}} \approx \frac{F_y \lambda}{2Nb}. \tag{11}$$

Hence, image resolution in azimuth is finer at higher frequencies. For constant subaperture widths, this resolution becomes coarser with increasing depth, as seen on Fig. 1. For a constant f-number subaperture, azimuthal width of the receive focus is unchanged with depth. Hence, azimuthal resolution stays the same even at greater depths, as seen in Fig. 2.

B. Simulated passive images of multiple bubbles

In a clinical or experimental application, an ability to image multiple bubbles is needed. Analytic expressions, derived above, can be used to assess passive imaging performance in the presence of emissions from multiple bubbles. Figure 3(a) is a simulated image of five acoustic sources with emissions in the frequency range 6.3–6.7 MHz (similar to experiments described below). For simplicity, it is assumed that all the sources continuously emit acoustic energy from their respective locations. The acoustic emission is assumed to be a stationary process, i.e., the temporal average of the emission energy stays constant during the formation of the entire image. These five sources are located at positions (azimuth mm, range mm): (−12,40), (−10,40), (0, 10), (0, 40), (0, 70). The source closest to the array at 10-mm depth can be resolved. However, the other two sources deeper on the axis cannot be seen very clearly on the image. The two off-axis sources, which are at the same depth and separated in the azimuth by 2 mm, can be clearly resolved. The azimuthal

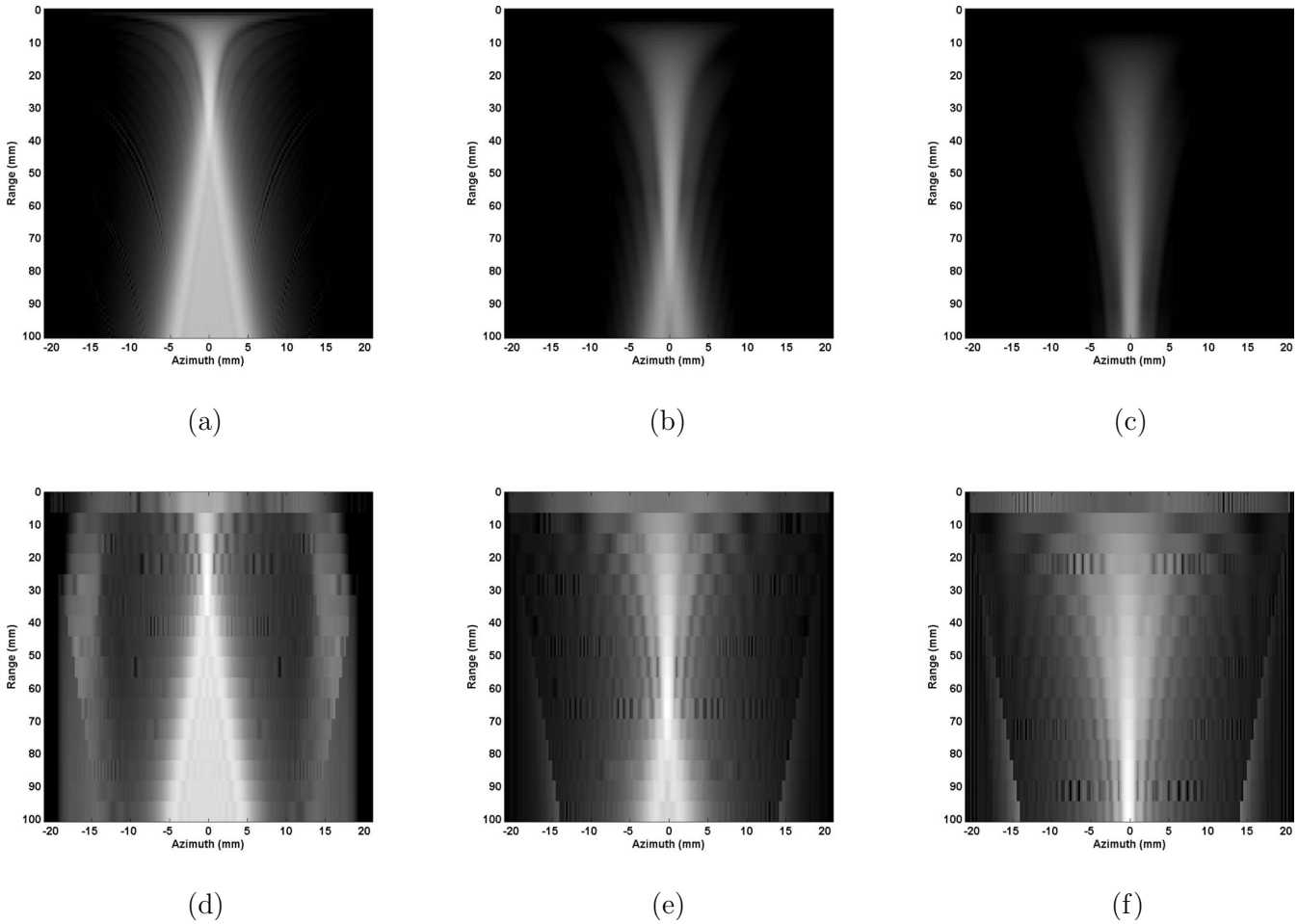

FIG. 2. Computer simulations for passive images created using a constant f-number (7.1) subaperture are shown here. Except for the subaperture sizes, images were created using the same simulation methods, focus positions, and source locations as the corresponding panels in Fig. 1.

width of the synthetic focus is smaller than the range width, especially at greater depths. This leads to better resolution in the azimuthal direction.

During HIFU ablation, cavitation activity is known to occur near the focal region, which may result in a cluster of active microbubbles.[16] It is important to determine whether passive imaging can be employed to estimate the location and size of such a cloud of multiple acoustic sources. Figure 3(b) has a simulated image of 25 sources emitting energy between 6.3 and 6.7 MHz. This frequency range is consistent with experiments in saline solution, sonicated with 520-kHz ultrasound. The 25 point-sources are randomly placed in the image plane (zero elevation) between −7 to −3 mm in azimuth and 31–41 mm in range. On this image, the azimuthal position of the bubble cluster can be identified more readily than its position in depth direction. To test whether the passive image is consistent with the location of the simulated bubble cluster, the brightness value of the passive image [Eq. (7)] was averaged between depths 31 and 41 mm for the entire image width. This yielded the azimuthal distribution of the averaged brightness value shown in Fig. 3(c). The number of point-sources at a given azimuthal location was represented by a histogram, shown in Fig. 3(c). For comparison, the azimuthal distribution of brightness value on the passive image and the bubble location histogram were normalized and scaled between 0 and 1. The azimuthal brightness distribution was consistent with this histogram. A similar analysis was performed in the range (or depth) direction. In Fig. 3(d), the passive image brightness value was averaged between −7 and −3 mm azimuth for all depths and compared with the histogram for range locations of the point-sources. Greater agreement is seen between the azimuth-dependent emission energy and source distribution in Fig. 3(c), compared to the corresponding depth-dependent distributions in Fig. 3(d).

IV. EXPERIMENTAL METHODS

Experiments were conducted to test passive cavitation imaging methods in free-field and tissue media. The overall experimental set up is shown Fig. 4. Details of experimental system components, experimental configurations, and data processing methods are presented below.

A. Ultrasound imaging system

Passive imaging was performed with a 192-element linear array with center frequency of 7.5 MHz, array element dimensions of 7×0.195 mm^2 (elevation × azimuth), and pitch of 0.22 mm (L7, Ardent Sound, Mesa, AZ), and controlled by the Iris 2 imaging system (Ardent Sound, Mesa,

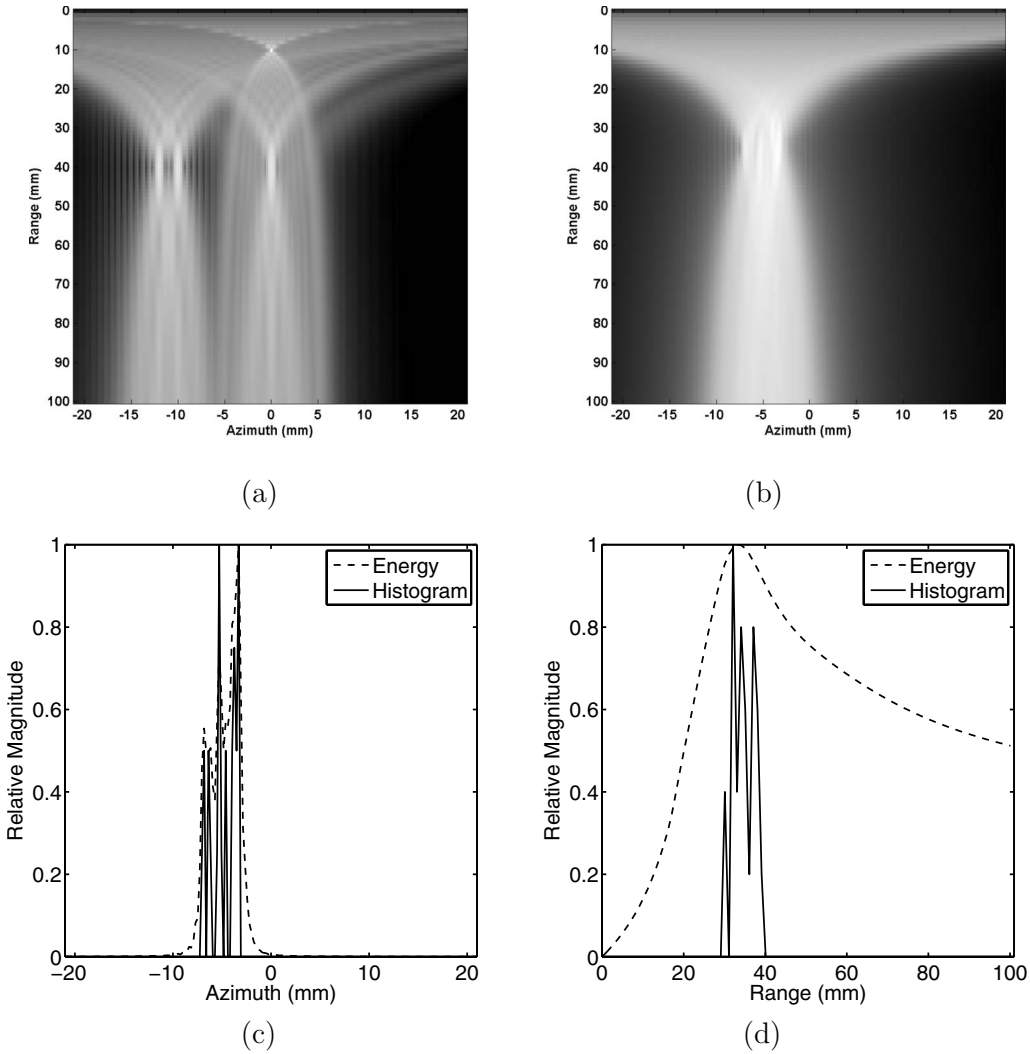

FIG. 3. Point-sources represented in this figure were assumed to emit acoustic energy between 6.3 and 6.7 MHz (64-element subapertures). (a) Simulated image of five point-sources at (azimuth mm, range mm): (−12,40), (−10,40), (0, 10), (0, 40), (0, 70). (b) Simulated image of a cluster of 25 point-sources placed randomly in the image plane between −7 and −3 mm in azimuth, and 3141 mm in depth. (c) Comparison between depth-integrated simulated image brightness as a function of azimuth, and the azimuthal distribution of point-sources. (d) Comparison between azimuth-integrated simulated image brightness as a function of range, and the range distribution of point-sources. Passive cavitation images are plotted with a 40 dB dynamic range.

AZ). The imaging array was focused in elevation (shorter array dimension) with an acoustic lens (focal length = 25 mm). This made it less sensitive to out-of-plane acoustic emission during cavitation experiments. This array was operated under constant width subaperture (64-elements) and constant *f*-number subaperture (7.1) beamforming configurations, with 16 receive focal zones (length of 6.2 mm) and a total image depth of 101 mm. Image frames were captured at

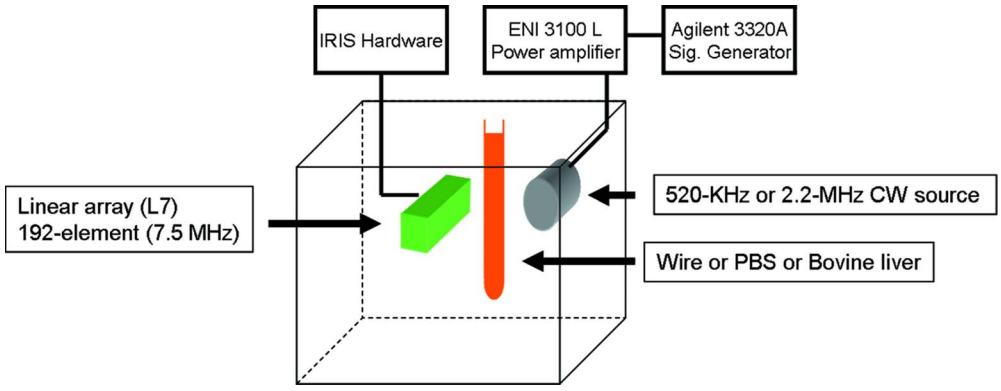

FIG. 4. (Color online) Experimental setup: CW ultrasound sources sonicate a 1-mm steel wire, PBS and bovine liver, while a 192-element linear array captures passive images.

a rate of 28 Hz and the beamformed rf lines were digitally recorded using a personal computer based A/D card (Compuscope CS14200, Gage Applied, Montreal, Canada) at a sampling frequency of 33.3 MHz.

B. Transducers

Two CW ultrasound sources were used for sonication. Their specifications were (1) C302, 520 kHz, 1 in. diameter, unfocused (Panametrics, Waltham, MA) and (2) IX327, 2.2 MHz, 4×15 mm^2 (UTX, Holmes, NY), cylindrically focused at a depth of $\approx$41 mm. They were driven with a signal generator (33220A, Agilent, Santa Clara, CA) and a power amplifier (3100L, ENI, Bell Electronics, Kent, WA).

During the initial experiments, dealing with cavitation detection in free-field, a single-element passive cavitation detector was used in conjunction with the imaging array to record bubble emissions. This was a cylindrically focused transducer, made from PVDF material, 0.75 in. diameter, center frequency of 10 MHz, and focal depth of 19 mm (Valpey Fischer 46654, Hopkinton, MA). The signals received by this detector were amplified by a low-noise preamplifier (SR 560, Stanford Research Systems, Sunnyvale, CA) and then digitally recorded (sampling rate = 50 MHz) using a Waverunner 6050A oscilloscope (LeCroy Corp., Chestnut Ridge, NY).

C. Transducer calibration

Each source transducer was calibrated using a scanning hydrophone system. This system consisted of a motorized three-axis translation assembly (NF90 series, Velmex Inc., Bloomfield, NY), with a 0.02 mm precision, to move needle hydrophones (0.5 mm diameter; SN 1239, Precision Acoustics Ltd., Dorchester, United Kingdom) through the acoustic fields. The signals measured by the hydrophone were recorded on a digital oscilloscope (Waverunner DSO, LeCroy Corp., Chestnut Ridge, NY) and stored on a desktop computer. The entire system was controlled by subroutines written in LABVIEW (National Instruments Corp., Austin, TX), executing on the same computer.[34]

D. Experiment configurations

Passive cavitation imaging was tested using three different experimental configurations. The source transducers were used to induce cavitation in PBS solution and *ex vivo* bovine liver. The ultrasound sources, imaging array and samples were suspended in a glass tank filled with de-ionized, degassed ($\%O_2 < 35$) water, filtered to keep the particle size less than 0.2 μm. To align the single-element transducers, they were driven in a pulse-echo mode by an ultrasound analyzer (5052UAX50, Panametrics, Waltham, MA) and a steel disk ($\approx$2 mm in diameter) was used as a target. The position of the steel disk, relative to the ultrasound array, was ascertained from B-mode images. These B-scans were obtained by the same array used for passive imaging.

1. Prediction of acoustic source position

Measurement of emissions from a single emission source could assist in validating the passive imaging models, described above. Instead of creating a single bubble or using a hydrophone as a point-source,[35] for simplicity, scattered ultrasound from a 1-mm steel wire, orthogonal to the image plane, was recorded passively. The wire was moved to 21 distinct positions in the image plane and passive images were captured. Scattered harmonics of the 520-kHz fundamental between 5.2 and 9.36 MHz (bandwidth of the L7 array) were resolved with a constant f-number configuration.

2. Cavitation imaging in PBS

To test passive imaging of cavitational emissions from a cluster of bubbles, cavitation activity was created by sonicating PBS solution in a 30-mm latex condom, placed orthogonal to the image plane. The PBS solution was exposed to 520-kHz, continuous-wave ultrasound between 0 and 0.15 MPa (peak-negative). During some initial experiments, passive cavitation detection was also performed with a 10-MHz transducer, along with passive imaging. Axes of the single-element detector and the source were perpendicularly aligned in the image plane.[23] Signals values recorded with the source transducer turned off were used as reference noise levels.

3. Cavitation imaging *in* ex vivo *bovine liver*

To assess passive cavitation imaging in sonicated soft tissue, *ex vivo* bovine liver was exposed to 2.2-MHz, continuous-wave, focused ultrasound. The source was aligned using a pulse-echo technique with the propagation direction orthogonal to the image plane and the source focus at 20 mm depth on the imaging array axis. The sonication amplitude was increased from 0–1.96 MPa peak-to-peak pressure, corresponding to 0–0.58 MPa peak-negative pressure. These pressures were measured in the free-field using the scanning hydrophone system mentioned above.

For the experiments described here, four samples of fresh bovine liver, less than 12 h *postmortem*, were used. Each sample was cut to a size of $7 \times 3 \times 3$ cm^3. One side (7×3 cm^2) of this sample had the liver capsule intact and this side faced the source transducer. During the four experiments, which were conducted over a three hour period, the bovine liver was placed in saline over ice, to minimize tissue decay and formation of any gas bubbles. Initial temperature of the tissue samples was between 17 °C and 21 °C. To prevent significant temperature increase due to absorption of the source ultrasound, the 2.2-MHz transducer was driven for single cycles of 4 s, and then turned off for at least 55 s. This on/off sequence was repeated for 16 increasing acoustic pressure levels. After each exposure the tissue sample was sliced systematically near the spatial position of the HIFU focus to confirm that there was no tissue coagulation.

No temperature measurements were made during the exposure. The temperature rise for these exposures, estimated through numerical methods, was 2.93 °C for one duty cycle at the highest sonication amplitude. Section VI contains

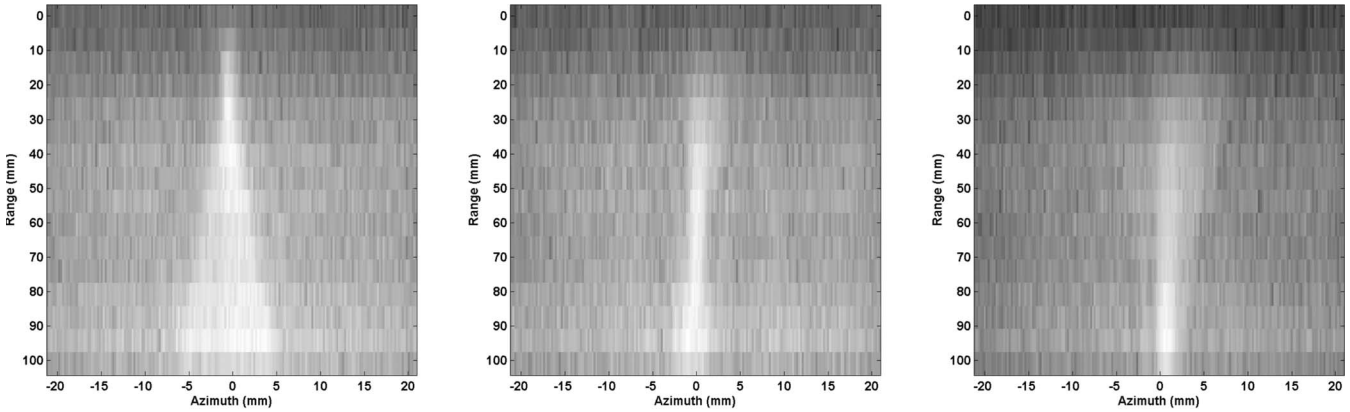

FIG. 5. (a) Passive images of 520-kHz ultrasound scattered from a 1-mm steel wire located at 20-mm depth, (b) 55 mm and (c) 90 mm. A constant *f*-number (7.1) subaperture was employed. Energy in the source harmonics (5.2–9.36 MHz) was integrated. Passive cavitation images are plotted with a 40 dB dynamic range.

some information about the effect of temperature on cavitation activity and calculations for the estimated temperature rise.

E. Power spectrum estimation

To form passive cavitation images, each rf *A*-line was beamformed using receive foci at multiple depths. The focus position corresponds to a passive image point and is at the center of a focal zone. The brightness value at an image point is equal to the integrated emission energy contained in the bounding focal zone. To calculate the emission energy, power spectra were estimated for the beamformed rf *A*-line signals within each focal zone. Energy in frequency bands consistent with inertial and stable cavitation was integrated to form separate images for the two regimes.

Estimation of power spectra was done over a total of 36 image frames, each consisting of 192 rf lines (101-mm image depth). Each rf line was beamformed with 16 equally spaced receive foci. Each focal zone consisted of 276 data points, with the synthetic focus positioned at the center of the zone, corresponding to a point on the passive image. Hence, every passive image had 192 × 16 points (number of rf lines per frame × number of focal zones; azimuth × range). For each focal zone, the sampled acoustic emission segments from nine consecutive frames were concatenated to form 2494-point signals, allowing power spectrum estimation with high frequency resolution. No temporal windowing function was applied. Power spectra were estimated by averaging the squared magnitude of the discrete Fourier transform for 4 of these 2484-point signals.

To obtain a single passive cavitation image (created only with subharmonic or broadband frequencies), 36 image frames (unfiltered images created from rf lines) were utilized. The frame rate for this capture was 28 Hz, so that the total data set required to form a single passive cavitation image was acquired over 1.3 s. The acquisition of each rf line is asynchronous, but the assumed stationarity of cavitational emissions allowed these individual lines to be juxtaposed, forming a meaningful passive cavitation image. Stationarity implies that the temporal average of cavitational emission energy radiating from a specific localized volume, which contains a bubble cluster, remains constant over the total data acquisition time. Hence, it is assumed that while the same bubbles do not necessarily cavitate over the entire acquisition time, the average energy of cavitational acoustic emissions remains constant over the entire acquisition time.

Power spectra were computed for acoustic emission signals recorded by the 10-MHz detector using the periodogram method. A total of 38 signal traces, each of length 100 μs sampled at 50 MHz, were analyzed. A discrete Fourier transform was computed for each trace, after applying a 2500-point rectangular window. Squared magnitudes of these Fourier transforms were averaged across all the traces.

V. EXPERIMENTAL RESULTS

Passive cavitation images captured using the three experimental configurations described above are presented in this section.

A. Prediction of acoustic source position

Images formed from ultrasound energy scattered by a steel wire are shown in Fig. 5 constant *f*-number subaperture). The wire was placed at depths of 20, 55, and 90 mm. These images are consistent with the simulation results shown in Fig. 2, for similar imaging parameters. This wire target was moved in the imaging plane to 21 known positions and its position was estimated from the passive images. To estimate the azimuthal location of the wire, the image grayscale value was averaged along the depth direction for all 192 azimuthal points. The position of maximum magnitude for this averaged value was taken as an estimate of the wire's azimuthal position. The location of maximum grayscale value in the range direction, at the estimated azimuth of the wire, was taken as an estimate of the wire's range position. The resulting rms error in predicting the azimuthal location was 0.9 mm and the corresponding range prediction error was 17.2 mm. The range position was consistently overesti-

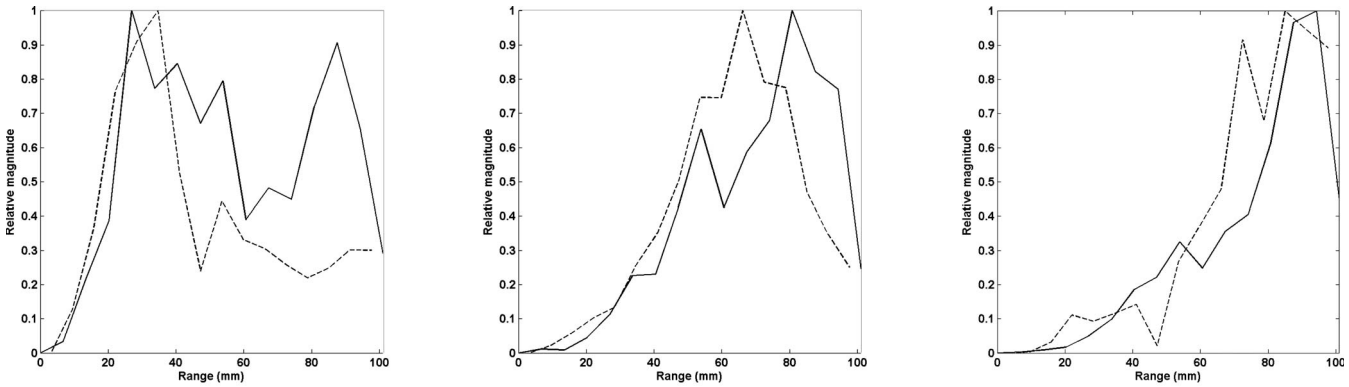

FIG. 6. Image magnitude along the array axis, plotted with respect to the range dimension, for representative simulation (---) and experiment (—) cases. The depth location of simulated point-sources and wire target (in experiment) were (a) 20 mm, (b) 55 mm, and (c) 90 mm.

mated in the passive images, as shown in Fig. 2. Also, consistent with simulations, the image resolution is coarser in range than azimuth.

The wire target employed in these experiments emulated a localized acoustic emission source. The L7 imaging array was focused in elevation (smaller dimension of the array) with an acoustic lens. Hence, the array was less sensitive to acoustic scattering from portions of the wire outside the imaging plane. The resulting effective source, although localized in space, was a rough approximation of a single point-source. This setup more closely mimicked a localized cluster of acoustic sources, similar to a cavitating bubble cloud, likely to be encountered by passive imaging methods during a scenario such as ultrasound ablation. The finite dimensions of this effective source could explain the overestimation of the wire's range position. The target acts as a group of sources and leads to a broader energy pattern along the range direction compared to the energy pattern of individual sources. This discrepancy may cause substantial errors when estimating the range location of spatially distributed acoustic emission sources. Figure 6 illustrates axial variation in passive image magnitude for simulated point-sources and acoustic scattering from the wire target.

B. Cavitation imaging in PBS

To image confirmed cavitation activity, bubbles were nucleated in PBS solution, using a 520-kHz source. During some initial experiments, acoustic emissions were recorded using a single-element detector (10 MHz) along with the passive images. Power spectra were computed for the emissions detected by the single-element transducer and the linear array. Broadband emissions consistent with inertial cavitation were observed in the data acquired by both methods (Fig. 7). These experiments served to verify that the imaging array was indeed detecting cavitation activity.

Following this initial confirmation, the single-element detector was not employed in further testing. Bubble activity was verified from B-mode imaging instead. When sonication amplitude was increased above 0.13 MPa (peak-negative pressure), echogenic bubbles were seen on B-mode images. During sonication at 520 kHz, echogenic bubbles would appear inside the PBS solution initially (away from the container walls). Due to acoustic radiation force, these bubbles would be pushed toward the distal wall of the container, where they would accumulate [see Fig. 8(a)] and cavitate for several minutes, as confirmed from B-scan images. The source pressure was increased from 0–0.15 MPa (peak-negative pressure). At each pressure value, a B-scan was captured, and then passive images were recorded using 64-element subapertures. Following these two steps, a B-scan was captured again. The initial and final B-scans did not show any significant change in the position or size of the bubble cloud, consistent with the assumption of stationary emission energy.

Power spectra were estimated in passive image focal zones, as explained above. For a given focal zone, energy contained in the 6.5-MHz bin, corresponding to an ultraharmonic frequency (12.5 × 520 kHz), was ascertained. The passive cavitation image point centered in this focal zone was then assigned the estimated energy level. This process was performed at every focal zone position to result in a 192 × 16 point passive cavitation image made from energy at 6.5 MHz. Similarly, separate images were formed from broadband emissions within 6.3–6.7 MHz (the 6.5-MHz ultraharmonic component was excluded). Representative images can

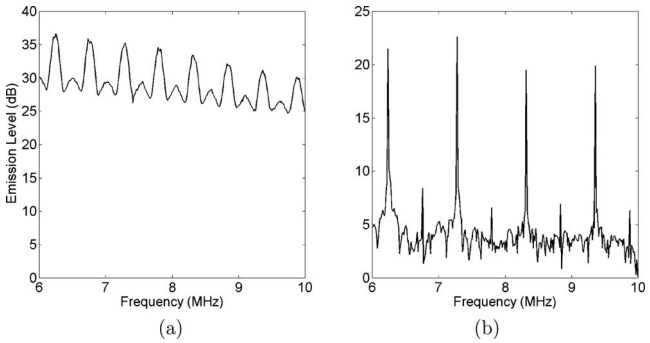

FIG. 7. Acoustic emission spectra from PBS solution sonicated with 520-kHz, cw ultrasound at 0.125 MPa (peak-negative pressure). Power spectra measured in dB relative to the measured noise floors were computed from (a) rf data acquired by the L7 array and (b) acoustic emission signals recorded by the single-element (10 MHz) detector.

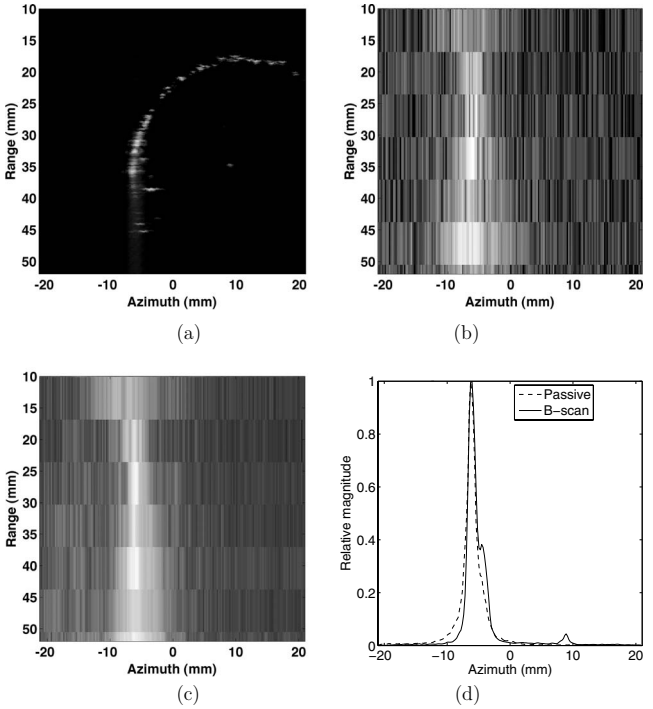

FIG. 8. Representative passive cavitation images in saline solution due to 520-kHz CW ultrasound 0–0.15 MPa (peak-negative): (a) B-scan showing a cavitating bubble cloud, (b) co-registered passive cavitation image formed from ultrahar-monic emissions (6.5 MHz), and (c) co-registered passive cavitation image formed from broadband emissions (6.3–6.7 MHz). (d) Comparison between B-scan and passive image brightness levels integrated between 31 and 41-mm depth, across all azimuths. Passive cavitation images are plotted with a 30 dB dynamic range.

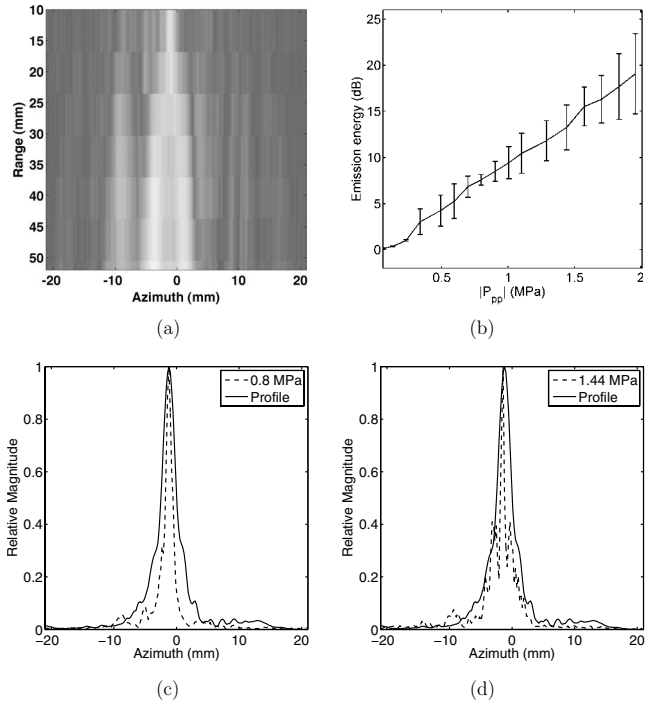

FIG. 9. (a) Representative passive cavitation image using broadband emissions (8–10 MHz) from bovine liver sonicated with 2.2-MHz, CW, focused ultrasound at 0.8 MPa peak-to-peak pressure amplitude (0.38 MPa peak-negative pressure). (b) Spatially integrated emission energy as a function of sonication amplitude, plotted as mean ± st. dev. (c) Comparison of emission amplitude at 20-mm depth with measured beam profile at 0.80 MPa (peak to peak) sonication pressure. (d) Comparison of emission amplitude at 20-mm depth with measured beam profile at 1.44 MPa (peak to peak) sonication pressure. Passive cavitation images are plotted with a 40 dB dynamic range.

be seen in Fig. 8. In 11 trials, where sonication pressure exceeded 0.125 MPa (peak-negative), half-order $(nf_0+f_0/2)$ ultraharmonic energy emissions were detected in one case, while one-third $(nf_0+f_0/3)$ and two-third order $(nf_0+2f_0/3)$ ultraharmonics were observed in several other runs. These could possibly result from stable cavitation activity.[3] Broadband emissions, possibly due to inertial cavitation, were recorded in all 11 trials.

A region-of-interest (ROI) was chosen between the 31-41-mm depth and across all azimuths (entire image width), on both the B-mode and broadband-emission images. A depth-integrated image value was computed as a function of azimuthal position by summing the image magnitude along depth in the ROI, for both images. B-mode image magnitudes were obtained from pulse-echo rf data. Broadband-emission image magnitudes were obtained from filtered, passive-rf signals. A representative comparison of azimuthal distributions of depth-integrated image magnitudes can be seen in Fig. 8(d). Pearson's correlation coefficient was computed for these two distributions for 11 trials. It was found to be statistically significant for all cases and the correlation coefficient value was always greater than 0.85. This confirms the possibility of predicting the azimuthal location of bubble clusters from passive images, consistent with computer simulations (Fig. 3). Here, the passively acquired rf signals were filtered to include emission energy in bands corresponding to stable and inertial cavitation (ultraharmonic or broadband frequencies) from mechanically active microbubbles. Conversely, harmonic scattering from larger bubbles could also be imaged by appropriately filtering the passively received rf signals.

C. Cavitation imaging in *ex vivo* bovine liver

Fresh bovine liver was exposed to a 2.2-MHz, focused source and passive images were captured with the L7 array. Broadband-emission energy was detected and spatially resolved using 64-element subapertures [Fig. 9(a)]. The broadband frequency range between 8–10 MHz, sufficiently different than the fundamental frequency of 2.2 MHz, was utilized. The imaging array has a center frequency of 7.5 MHz and is sensitive up to 10 MHz. To ensure that the fourth harmonic (8.8 MHz) was filtered out, acoustic energy in the band 8.63–8.93 MHz was removed. Figure 9(a) clearly indicates the ability of this imaging modality to obtain spatial information about acoustic emissions from the tissue. Broadband-emission energy integrated across the entire image increased monotonically with the sonication amplitude [Fig. 9(b)]. This increase in the broadband-emission energy could be related to inertial cavitation activity. However, broadband-emission levels estimated in this manner may also contain contributions from spectral side lobes of fourth-harmonic signals nonlinearly scattered from bubbles in the tissue samples.

Broadband-emission images were also employed to ascertain the azimuthal position of the source focus. The location of the maximum brightness value at 20-mm depth was

assigned the value of source focus azimuth. Source focus azimuths (mean ± st. dev.) for the four samples, based on 16 sonication levels per sample, were −1.02 ± 0.5, −1.05 ± 0.46, −3.69 ± 0.46, and −1.57 ± 0.9 mm. The position estimate from sample 3 is different, but the other cases show fair agreement. B-mode images of sample 3 showed accumulation of echogenic gas bubbles at several locations away from the source focus. It was observed that the largest emissions for sample 3 emanated from these bubbles localized outside the sonication focal region, causing the discrepancy in source focus localization from the passive image. This result could be significant for an application such as HIFU ablation monitoring, where tissue coagulation may also happen away from the source focus. It should be noted that the standard deviation for all samples was less than 1 mm, indicating good image resolution in the azimuthal direction. Range location of the acoustic emissions cannot be determined as reliably as their azimuthal position. However, if visually compared, the passive image in Fig. 9(a) is more similar to the simulated image of a point-source at 20-mm depth, as seen in Fig. 1(d) than to simulated images of point-sources at greater depth in Figs. 1(e) and 1(f). This implies that broadband acoustic emissions emanated from within the tissue samples close to the 20-mm depth on the image, corresponding to the source focus position (a more quantitative analysis follows in Sec. VI).

Azimuthal broadband image brightness distribution was compared with the source beam shape, as measured in free-field by a scanning hydrophone system. Figures 9(c) and 9(d) show a comparison between relative magnitudes of source pressure and broadband-emission energy with respect to azimuth, both measured for the same spatial region at 20-mm depth in the image plane. Azimuthal brightness distribution on the broadband-emission image is consistent with the measured beam shape. With an increase in sonication amplitude, the brightness pattern on broadband-emission images broadens azimuthally. At lower sonication pressures, broadband emissions occur mainly in the main lobe, resulting in a broadband emission pattern narrower than the source beam pattern [Fig. 9(c)]. For higher sonication amplitudes, the emission pattern broadens and is closer in width to the source beam pattern [Fig. 9(d)].

These results suggest that passive cavitation imaging may be useful for imaging or mapping therapeutic ultrasound beams. The relation between broadband emissions and source pressure amplitude, as seen in Fig. 9(b), may be utilized to obtain a mathematical function between the two quantities. It may also be possible to ascertain in situ pressure distributions based on the passive cavitation image brightness by exploiting such a numerical mapping.

VI. DISCUSSION

Passive cavitation imaging is examined here with a future goal of application in real-time guidance and monitoring of ultrasound ablation. Hence, the acoustic emissions detected from sonicated bovine liver samples are discussed. Similarly, strengths, limitations, and possible improvements for passive cavitation imaging are also discussed.

A. Tissue emissions and the inertial cavitation threshold

Experimental results presented above indicate a monotonic rise in cumulative broadband emissions energy with increasing sonication amplitudes [Fig. 9(b)]. In other experimental studies with sonicated Optison solutions[36,37] and ablated tissue *in vitro*,[23] a similar trend has been observed. Other researchers also report a rise in the number of macroscopic bubbles in muscle[14] and gel phantoms[38] with increasing acoustic pressures. During the experiments reported in Sec. V, broadband emissions were recorded over a prolonged period. This can result from pre-existing gas and microbubbles in the tissue samples, as evidenced in some earlier publications where similar CW sonications were employed.[14,39] Such cavities can grow through rectified diffusion[40] to a size where they undergo violent inertial collapse.[41] The fragments resulting from such a transient event may produce smaller bubble nuclei, "providing cavitation with a self-enhancing mechanism of positive feedback"[3] due to repeated collapse and coalescence of the bubbles.[42,43]

Cavitation-related broadband emissions occur above threshold pressure amplitude that depends on factors such as viscoelastic properties of the medium, prevalence of pre-existing nuclei and dissolved gas content, among others. An upper bound for this threshold, given an optimally sized bubble and single cycle excitation at 2.2 MHz, is close to 0.47 MPa (peak-negative).[44] It is also documented that inertial cavitation thresholds could be 3–40 times higher in tissue than in water.[45] However, for the CW exposure conditions employed here, inertial cavitation may occur at lower pressure values due to the presence of pre-existing nuclei and their growth through rectified diffusion. Also, the liver samples used in the experiments contained blood and saline solution around the tissue, with several possible cavitation nucleation sites.

It is estimated through simulations that small (<3 μm) bubbles may grow through rectified diffusion.[46] Pre-existing nuclei under 3 μm size, subjected to multiple cycle exposures with frequencies between 2 and 3 MHz, may have the threshold for rectified diffusion as low as 0.09 MPa (peak-negative).[46,47] Hence, bubbles grown by rectified diffusion may either undergo inertial collapse or cause nonlinear scattering of source harmonics. A peak-negative pressure of 0.09 MPa was eclipsed in the main lobe of the focused source beam for most exposure conditions, presented above. The pressure values achieved in the first side lobe, about 1/7 of the main lobe. It is likely that pressure in the side lobes was close to this threshold value, especially at higher sonication amplitudes such as 1.44 MPa (peak-to-peak). This could lead to broadband emissions in the side lobes at such pressure levels (see Fig. 9).

Temperature changes in the tissue may alter the acoustic pressure threshold values for inertial cavitation or rectified diffusion, due to either the dissolved gas coming out of solution or coagulation of liver samples due to hyperthermia. An estimate of the temperature rise was calculated for the exposure conditions employed during the tissue experiments (reported above). This was achieved by solving a simplified Pennes bio-heat transfer equation at the location of the 2.2-

MHz source focus, with acoustic nonlinear propagation, thermal diffusion, and perfusion losses ignored.[19] This yielded a "worst case" estimate for temperature rise. The value of temperature increase was 16.24 °C at the end of 16 sonications of 4 s on/55 s off, where the pressure amplitude was sequentially increased between 0 and 1.96 MPa (peak-to-peak pressure measured in free-field). For the duty cycle with the highest sonication amplitude, the temperature increase was 2.93 °C. The actual temperature rise during the experiments would be less than this estimate, given the conductive heat dissipation. With an initial tissue temperature close to 20 °C, it was likely that the temperature elevation caused by the HIFU source would not result in thermal coagulation.[19] While no coagulation was observed when the tissue samples were sliced after exposure, the source ultrasound beam could possibly have caused localized temperature elevations in the tissue. These can result in increased nucleation events and a reduced inertial cavitation threshold.[45] The relation between cavitation in tissue, the concomitant emissions, and ultrasound pressure needs further elucidation.

B. Ablation monitoring

The strong dependence of bubble activity on temperature and physical properties of the medium make passive cavitation imaging a potential tool for ablation monitoring. The authors have previously explored some preliminary statistical frameworks that relate these quantities.[48] Spatially resolved bubble emissions may enable real-time tracking of cavitation-related phenomena such as "tadpole" lesioning during HIFU ablation.[17] Future studies may include ultrasound ablation experiments with passive imaging where position-dependent cavitation will be used as a measure of local heat deposition and tissue coagulation.

Cavitation activity, as well as vaporization due to boiling, may occur during ultrasound ablation. Passive imaging may be used for ablation monitoring by tracking both these phenomena. Experimental evidence suggests that low-frequency emissions arise due to tissue boiling. Resolution in passive images depends on the emission frequency and images from such kilohertz-frequency emissions will probably have low resolution. However, tissue boiling may be monitored by imaging the source harmonics scattered by the resulting vapor bubbles.

Based on the consistent agreement between passive images and HIFU beam shapes, as presented in Sec. IV, passive imaging technique may potentially be employed to align therapeutic ultrasound beams during clinical procedures.

C. Improving cavitation imaging performance

Cavitation imaging performance can be improved if the range location of the acoustic emissions can be ascertained. Although range resolution of passive cavitation images is limited, spatial correlation between acquired passive images and simulated images may be exploited to estimate source range locations more accurately. A possible metric R for this may be based on the Pearson product-moment correlation coefficient:[49]

$$R(y_s,z_s) = \frac{\sum_{\forall Y}\sum_{\forall Z}(I_a(Y,Z)-I'_a)(I_s(y_s,z_s,Y,Z)-\bar{I}_s)}{\sqrt{\sum_{\forall Y}\sum_{\forall Z}(I_a(Y,Z)-\bar{I}_a)^2}\sqrt{\sum_{\forall Y}\sum_{\forall Z}(I_s(Y_s,z_s,Y,Z)-\bar{I}_s)^2}}, \quad (12)$$

where I_a is the acquired image and I_s is the simulated image of a point-source at (y_s,z_s). The value of (y_s,z_s) that maximizes R can be used as an estimate of the source location. If this function R is computed for Fig. 9(a) and each of the simulated images in Figs. 1(d)–1(f), the value of R comes out to be 0.54 for point-source location (0,20), 0.33 for point-source location (0, 55), and 0.37 for point-source location (0, 90). This result is consistent with the location of the HIFU focus, which was aligned to position (0, 20) by the pulse-echo method mentioned above. Development of such algorithms is beyond the scope of this paper.

While modeling-based approaches may help in improving cavitation imaging performance, modifications to the ultrasound imaging hardware may potentially achieve better results. In the Iris 2 system described above, the beamformed rf A-lines are acquired sequentially. If multiple A-lines were recorded with parallel channels, it would be possible to receive cavitational emissions synchronously. This would enable the use of cross-correlation based methods[26] or inverse source reconstruction techniques.[50] Such parallel receive hardware would also make it possible to image short-lived cavitational events that occur during procedures such as lithotripsy. A lithotripter produces a shock wave which leads to a single transient cavitational event. Passive sensing of such an event with multiple receive channels would potentially provide effective range gating.

VII. CONCLUDING REMARKS

In this paper, passive cavitation imaging was introduced and the point-spread function of a cavitation image was derived. Passive images were simulated for both constant sub-aperture width and constant f-number beamforming, which indicated that the bubble emissions could be resolved accurately along the array azimuth. Passive imaging was implemented on a 192-element ultrasound array and was successfully tested by imaging harmonic scattering from a wire. Cavitational emissions from microbubbles nucleated in saline solution and broadband emissions from bovine tissue were also imaged. The distribution of azimuthal energy in the broadband emission images of *ex vivo* tissue was compared with the beam shape of the ultrasound source. The consistent agreement between the two indicates a strong possibility of mapping therapeutic ultrasound beams *in situ*, though several quantitative questions dealing with the direct relationships between sonication amplitude, tissue temperature, and passive image brightness need to be resolved.

ACKNOWLEDGMENTS

This work was supported by NIH Grant No. R21 EB008483 and the University of Cincinnati College of Medi-

cine Dean's Bridge Funding Program. Jonathan Kopechek is thanked for help with transducer calibration.

[1]R. E. Apfel, "Acoustic cavitation inception," Ultrasonics **22**, 167–173 (1984).
[2]H. G. Flynn, "Physics of acoustic cavitation in liquids," Phys. Acoust. **1**, 57–172 (1964).
[3]T. G. Leighton, *The Acoustic Bubble* (Academic, London/Academic, San Diego, CA, 1994), Chap. 4.
[4]A. Anand, L. Byrd, and P. J. Kaczkowski, "*In situ* thermal parameter estimation for HIFU therapy planning and treatment monitoring," Proc.-IEEE Ultrason. Symp. **1**, 137–140 (2004).
[5]L. A. Crum, "Cavitation microjets as a contributory mechanism for renal calculi disintegration in ESWL," J. Urol. (Baltimore) **140**, 1587–1590 (1984).
[6]R. K. Zemen, W. J. Davros, B. S. Garra, and S. C. Horri, "Cavitation effects during lithotripsy Part 1. Results of *in vitro* experiments," Radiology **177**, 157–161 (1990).
[7]R. O. Cleveland, "Acoustics of shock wave lithotripsy," in Renal Stone Disease 1st Annual International Urology Research Symposium (2007), pp. 311–316.
[8]S. B. Olsson, B. Johansson, A. M. Nilsson, C. Olsson, and A. Roijer, "Enhancement of thrombolysis by ultrasound," Ultrasound Med. Biol. **20**, 375–382 (1994).
[9]S. Datta, C. C. Coussios, L. E. McAdory, J. Tan, T. Porter, G. De Courten-Myers, and C. K. Holland, "Correlation of cavitation with ultrasound enhancement of thrombolysis," Ultrasound Med. Biol. **32**, 1257–1267 (2006).
[10]E. C. Everbach and C. W. Francis, "Cavitational mechanisms in ultrasound-accelerated thrombolysis at 1 MHz," Ultrasound Med. Biol. **26**, 1153–1160 (2000).
[11]E. C. Unger, T. Porter, W. Culpd, R. Labella, T. Matsunagaa, and R. Zutshi, "Therapeutic applications of lipid-coated microbubbles," Adv. Drug Delivery Rev. **56**, 1291—1314 (2004).
[12]K. Hynynen, "Ultrasound for drug and gene delivery to the brain," Adv. Drug Delivery Rev. **60**, 1209–1217 (2008).
[13]J. A. Kopechek, T. M. Abruzzo, B. Wang, S. M. Chrzanowski, D. A. B. Smith, P. H. Kee, S. Huang, J. H. Collier, D. D. McPherson, and C. K. Holland, "Ultrasound-mediated release of hydrophilic and lipophilic agents from echogenic liposomes," J. Ultrasound Med. **27**, 1597–1606 (2008).
[14]G. R. ter Haar and S. Daniels, "Evidence for ultrasonically induced cavitation *in vivo*," Phys. Med. Biol. **26**, 1145–1149 (1981).
[15]K. Hynynen, "The threshold for thermally significant cavitation in dog's thigh muscle *in vivo*," Ultrasound Med. Biol. **17**, 157–169 (1991).
[16]C. C. Coussios, C. H. Farny, G. R. ter Haar, and R. A. Roy, "Role of acoustic cavitation in the delivery and monitoring of cancer treatment by high-intensity focused ultrasound (HIFU)," Int. J. Hyperthermia **23**, 105–120 (2007).
[17]N. A. Watkin, G. R. ter Haar, and I. H. Rivens, "The intensity dependence of the site of maximal energy deposition in focused ultrasound surgery," Ultrasound Med. Biol. **22**, 483–491 (1996).
[18]L. Curiel, F. Chavrier, B. Gignoux, S. Pichardo, S. Chesnais, and J. Y. Chapelon, "Experimental evaluation of lesion predicting modeling in prescence of cavitation bubbles: Intended for high-intensity focused ultrasound prostate treatment," Med. Biol. Eng. Comput. **42**, 44–52 (2004).
[19]T. D. Mast, I. R. S. Makin, W. Faidi, M. M. Runk, P. G. Barthe, and M. H. Slayton, "Bulk ablation of soft tissue with intense ultrasound: Modeling and experiments," J. Acoust. Soc. Am. **118**, 2715–2724 (2005).
[20]V. Khokhlova, M. Bailey, J. Reed, B. Cunitz, P. Kaczkowski, and L. Crum, "Effects of nonlinear propagation, cavitation, and boiling in lesion formation by high intensity focused ultrasound in a gel phantom," J. Acoust. Soc. Am. **119**, 1834–1848 (2006).
[21]C. H. Farny, "Identifying and monitoring the roles of cavitation in heating from high-intensity focused ultrasound," Ph.D. thesis, Boston University, Boston, MA 2007).
[22]J. McLaughlan, I. H. Rivens, and G. R. ter Haar, "A study of cavitation activity in *ex vivo* tissue exposed to high intensity focused ultrasound," AIP Conf. Proc. **911**, 178–184 (2007).
[23]T. D. Mast, V. A. Salgaonkar, C. Karunakaran, J. A. Besse, S. Datta, and C. K. Holland, "Acoustic emissions during 3.1 MHz ultrasound bulk ablation *in vitro*," Ultrasound Med. Biol. **34**, 1434–1448 (2008).
[24]B. A. Rabkin, V. Zedric, and S. Vaezy, "Hyperecho in ultrasound images of HIFU therapy: Involvement of cavitation," Ultrasound Med. Biol. **31**, 947–956 (2005).
[25]C. C. Coussios, J. R. T. Collins, and A. P. Muckle, "Noninvasive monitoring and control of inertial cavitation dynamics during HIFU exposure *in vitro*," AIP Conf. Proc. **911**, 164–170 (2007).
[26]S. J. Norton and B. J. Carr, "Passive imaging of underground acoustic sources," J. Acoust. Soc. Am. **119**, 2840–2847 (2006).
[27]M. Gyongy, M. Arora, A. Noble, and C. C. Coussios, "A passive array technique for cavitation mapping during HIFU treatment," J. Acoust. Soc. Am. **123**, 3223 (2008).
[28]V. A. Salgaonkar, S. Datta, C. K. Holland, and T. D. Mast, "Passive imaging of cavitational acoustic emissions with ultrasound arrays," AIP Conf. Proc. **1113**, 73–77 (2009).
[29]T. L. Szabo, *Diagnostic Ultrasound Imaging: Inside Out* (Elsevier, Burlington, MA, 2004), Chap. 6.
[30]D. T. Blackstock, *Fundamentals of Physical Acoustics* (Wiley, New York, 2000), Chap. 10.
[31]A. D. Pierce, *Acoustics: An Introduction to its Physical Principles and Applications*, 2nd ed. (Acoustical Society of America, Melville, NY, 1989), Chap. 5.
[32]T. D. Mast, "Fresnel approximations for ultrasonic fields of rectangularly symmetric sources," J. Acoust. Soc. Am. **121**, 3311–3322 (2007).
[33]M. Abramowitz and I. A. Stegun, *Handbook of Mathematical Functions* (National Bureau of Standards, Washington, DC, 1972), Chap. 7.
[34]T. M. Porter, D. A. B. Smith, and C. K. Holland, "Acoustic techniques for assessing the optison destruction threshold," J. Ultrasound Med. **25**, 1519–1529 (2006).
[35]R. O. Cleveland, O. A. Sapozhnikov, M. R. Bailey, and L. A. Crum, "A dual passive cavitation detector for localized detection of lithotripsy-induced cavitation in vitro," J. Acoust. Soc. Am. **107**, 1745–1758 (2000).
[36]D. M. Hallow, A. D. Mahajan, T. E. Mccutchen, and M. R. Prausnitz, "Measurement and correlation of acoustic cavitation with cellular bioeffects," Ultrasound Med. Biol. **32**, 1111–1122 (2006).
[37]J. Tu, J. Hwang, T. Matula, A. Brayman, and L. A. Crum, "Intravascular inertial cavitation activity detection and quantification in vivo with Optison," Ultrasound Med. Biol. **32**, 1601–1609 (2006).
[38]S. Daniels, D. Blondel, L. A. Crum, G. R. ter Haar, and M. Dyson, "Ultrasonically induced gas bubble production in agar based gets: Part I, experimental investigation," Ultrasound Med. Biol. **13**, 527–539 (1987).
[39]P. F. Lewin and L. Bjorno, "Thresholds for rectified diffusion and acoustic microstreaming by bubbles in biological tissue," App. Science Reviews **38**, 25–35 (1982).
[40]A. I. Eller and H. G. Flynn, "Rectified diffusion during nonlinear pulsations of cavitation bubbles," J. Acoust. Soc. Am. **37**, 493–503 (1965).
[41]E. T. Ayme-Bellegarda, "Collapse and rebound of a gas-filled spherical bubble immersed in a diagnostic ultrasound field," J. Acoust. Soc. Am. **88**, 1054–1060 (1990).
[42]C. C. Church and E. L. Carstensen, "'Stable' inertial cavitation," Ultrasound Med. Biol. **27**, 1435–1437 (2001).
[43]D. F. Gaitan, L. A. Crum, C. C. Church, and R. A. Roy, "Sonoluminescence and bubble dynamics for a single, stable cavitation bubble," J. Acoust. Soc. Am. **91**, 3166–3183 (1992).
[44]R. E. Apfel and C. K. Holland, "Gauging the likelihood of cavitation from short-pulse low-duty cycle diagnostic ultrasound," Ultrasound Med. Biol. **17**, 179–185 (1991).
[45]C. C. Church and X. Yang, "A theoretical study of gas bubble dynamics in tissue," AIP Conf. Proc. **838**, 217–224 (2006).
[46]S. Datta, "The role of cavitation in enhancement of rt-PA thrombolysis," Ph.D. thesis, University of Cincinnati, Cincinnati, OH (2008).
[47]C. C. Church, "Prediction of rectified diffusion during nonlinear bubble pulsations at biomedical frequencies," J. Acoust. Soc. Am. **83**, 2210–2217 (1988).
[48]V. A. Salgaonkar, C. P. Karunakaran, J. A. Besse, G. Heinlein, S. Datta, C. K. Holland, and T. D. Mast, "Image-guided ex vivo liver ablation by unfocused ultrasound using passive cavitation detection," Proc. SPIE **6440**, Q1–Q10 (2007).
[49]J. L. Rodgers and W. A. Nicewander, "Thirteen ways to look at the correlation coefficient," Am. Stat. **42**, 59–66 (1988).
[50]Y. Kim and P. A. Nelson, "Optimal regularisation for acoustic source reconstruction by inverse methods," J. Sound Vib. **275**, 463–487 (2004).